# Development of a 3D model to predict curing dimensions and conversion rates of curable ceramic systems during stereolithography 3D printing process

D. Vallet, V. Pateloup, P. Michaud, T. Chartier

IRCER, Univ. Limoges, CNRS, UMR 7315, 12 Rue Atlantis, F-87000, Limoges, France

ARTICLE INFO

Keywords:
Stereolithography
Scattering
Dimensional accuracy
Conversion rate
Simulation model

ABSTRACT

To meet industry's expectations for manufacturing ceramic parts by stereolithography, a better comprehension of the process, in particular laser scattering through the ceramic slurry is mandatory. This knowledge makes it possible to define adapted printing conditions to control the dimensions, homogeneity of the conversion and mechanical properties of the green parts, in order to achieve better resolutions and optimize the properties of sintered parts. This approach is focused on the development of a 3D polymerization modeling for stereolithography process able to predict curing and associated thermal phenomena. First, a design of experiments is carried out to identify material-dependent parameters, calibrate and validate the model, then able to predict monomer conversion rates and dimensions after curing depending on manufacturing parameters. Finally, temperature variation and exposure homogeneity have been evaluated. These results will allow, in future studies, to interpret the differences of deformations and mechanical properties of green parts.

## 1. Introduction

Among all the existing additive manufacturing processes, stereolithography makes it possible to build complex and dense final ceramic parts with a high dimensional accuracy, excellent surface finish, good mechanical properties and without needing any mold [1–4]. Stereolithography is based on the selective polymerization of a reactive system consisting in a dispersion of ceramic particles in a UV curable resin (monomer and/or oligomer) with the addition of a photoinitiator. Stereolithography follows a layer by layer procedure with the insolation, by means of a deflected UV laser beam, of the proper cross-sectional pattern to harden in each layer [5–7].

The photoinitiator, submitted to the UV light, releases free radicals, resulting in the polymerization of the organic intergranular phase [8–10]. These radicals allow the initiation to occur and also the propagation, that is the progressive growth of polymer chains, by combining a monomer with a radical at the end of a polymer chain. A chain growth ends when two radicals react with each other, creating a stable non-reactive covalent bond during a step called termination [11].

Ceramic particles, in high concentration in the suspension (50-65% vol), are then trapped in the polymer matrix [12] conferring the mechanical strength to the green part. After completion of the part, the green object is debinded and sintered to confer the properties to the final part [13]. Stereolithography needs and applications have grown a lot since a decade, and this process is used in various fields like biomedical, luxury, electronics, casting molds and cores [14].

In order to master the stereolithography process, the interactions between the ceramic suspension and the laser have to be considered. The presence of ceramic particles in the slurry induces light scattering. Depending on the nature of the ceramic material, the particle size and shape, the volume fraction of particles and the density of energy delivered, light scattering will influence the conversion rate (or degree of conversion), the dimensions of the part and mechanical properties [12,15,16]. The optimization of the dimensional accuracy and properties of the green body then involves the understanding of the impact of scattering phenomena but also of manufacturing parameters (laser power, frequency and laser velocity, hatch spacing, layer thickness).

In this respect, and following a previous 2D model of J.Tarabeux [14], this study is focused on the development of a 3D model capable of predicting scattering phenomenon, conversion rate and temperature variation associated to polymerization in the volume during printing and dimensions of the green part, depending on laser, manufacturing and curable ceramic-based system parameters. This 3D approach allows the consideration of complex-shaped objects and some laser phenomena, like velocity variation close to edges and lasing angle rotation between layers, as well as allowing a more reliable and homogeneous conversion rate and warming-up simulation. A homogeneity study of the green body is also conducted to provide a better understanding of the influence of manufacturing parameters on final properties. In this respect, in order to construct a new 3D simulation model for a pulsed laser, a design of experiments is carried out. This knowledge will open the way to subsequent shrinkage and mechanical studies of green parts, then to properties of sintered ones.

## 2. Materials and methods

### 2.1. Presentation of the process

As a first step, a CAD file (Computer-Aided-Design) is generated, and then converted to STL format, to be sliced into several layers (according to chosen thickness, or to the cure depth) that will be printed during the stereolithography process [14].

The photopolymerizable paste is spread on a working support table using a scraper, then the laser beam scans selected areas, according to each layer's cross-sectional pattern, following lines at a given velocity $V_L$ and separated by a distance $h_s$ called hatch spacing. The Fig. 1 shows the trajectory of a pulsed laser following the x-axis direction and considering lasing angle of 0° and 30°. The working support is then moving down a layer thickness prior the deposition of the subsequent layer of suspension. These operations are repeated until the completion of

the part. In order to focus efficiently the laser beam onto the surface, a laser beam expender is placed after the laser source. This element allows to maximize the use of the scan system aperture and reduces the power density on the mirrors [17]. The beam is then accurately deflected by a scan head, composed of two galvanometer movable mirrors. Then, a F-Theta lens focusses the laser at the focal point. The optical system is shown in Fig. 2(a).

A commercial alumina ceramic curable paste (3D-Ceram Sinto, France) is used for all experiments. This paste consists in a suspension of micronic alumina particles (58% vol.) in an acrylate monomer-oligomer matrix, with the addition of a photo-initiator and a dispersant to stabilize the slurry. The polymerization is carried out by a pulsed UV laser with adjustable power and frequency, and a wavelength of 355nm, able to generate free radicals from the photo-initiator.

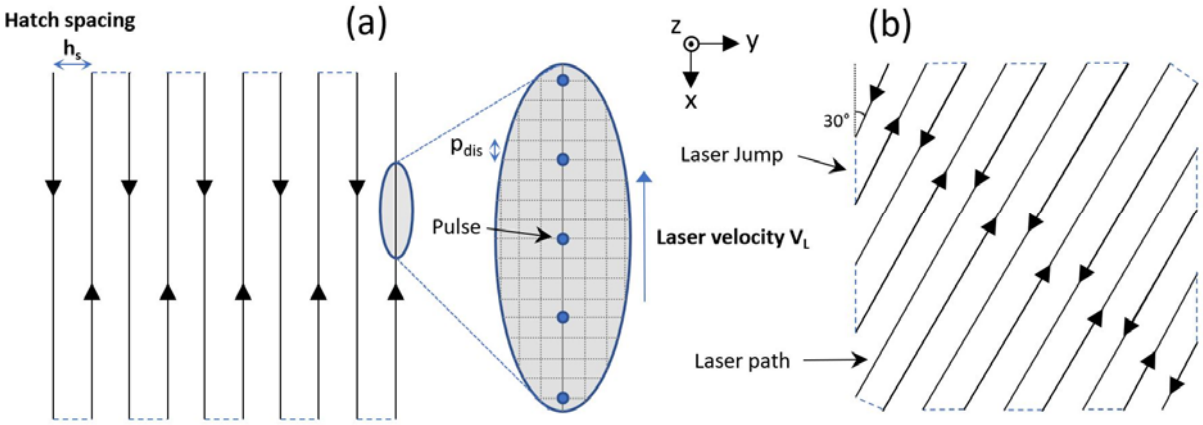


**Fig. 1.** Top view of a pulsed laser path in stereolithography (a) without any rotation, and (b) with a 30° rotation in lasing angle.

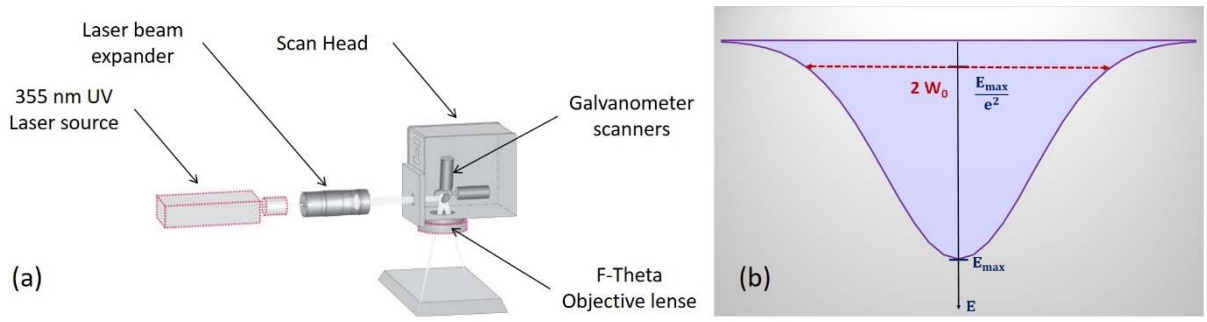


**Fig. 2.** (a) Optical system used in stereolithography and (b) 2D view of the resulting Gaussian exposure distribution [14,17]

2.2. Laser exposure

The laser intensity I (W/cm²) is defined as a power per surface unit. The beam is considered as a Gaussian beam, propagating along the z axis towards negative values [18]. As seen on Fig. 2(b), the maximum exposure $E_M$ is reached at $z = 0$. Therefore, the 3D intensity distribution I for a pulse is equal to [2]:

$$I(x,y,z) = \frac{2 * P_{pulse}}{\pi * W_0^2} * e^{\frac{z}{Dp}} * e^{\frac{-2(x^2+y^2)}{W_0^2}} \quad (1)$$

Where $P_{pulse}$ is the pulse power (or peak power), $W_0$ the laser beam radius at $z = 0$. $Dp$ is the penetration depth coefficient that denotes the laser attenuation due to light absorption during the propagation and corresponds to the depth where the intensity of the Gaussian laser beam is reduced by 1/e [14]. It is defined thanks to the Beer-Lambert law using the following relation [19,20] where ε and $c_{Abs}$ are respectively the molar extinction coefficient and the concentration of absorbing species, assumed constant:

$$Dp = \frac{1}{ln(10) * \varepsilon * c_{Abs}} \quad (2)$$

The laser intensity I is necessary to calculate the energy received at each point of the slurry and predict its curing, conversion rate and temperature. The exposure E (mJ/cm²) is linked to the intensity by the following relation [2] where $T_{pulse}$ is the pulse width (duration of a pulse):

$$E(x,y,z) = \int_0^{T_{pulse}} I(x,y,z)\,dt \tag{3}$$

Since the duration of the pulse is very low (~ns), the laser displacement during this time is negligible and I is time-independent because the beam covers the same area all along a pulse. In terms of simulation, this approximation is the main difference between pulsed and continuous lasers, often used in simulation models, in which the intensity I is time dependent and must be simplified by adding the laser velocity in the exposure formula [2,14]. Combining Eq.(1) and Eq.(3), we can express the energy received in three dimensions for one pulse:

$$E(x,y,z) = \frac{2 * P_{pulse} * T_{pulse}}{\pi * W_0^2} * e^{\frac{z}{Dp}} * e^{\frac{-2(x^2+y^2)}{W_0^2}} \tag{4}$$

$$E_M = \frac{2 * P_{pulse} * T_{pulse}}{\pi * W_0^2} \tag{5}$$

This exposure is illustrated in 2D by Fig. 2(b). By adding this energy for each pulse occurring during printing, a matrix of exposure $E_{total}$ is obtained. Since the energy distribution of a single pulse is deep enough, the conversion rate of a given layer increases during the lasing of subsequent close layers, leading to secondary, and even more, photopolymerization of the same volume [17,21]. $P_{pulse}$ and $T_{pulse}$ are calculated thanks to manufacturer data, and are linked to laser frequency $F_L$ and average laser power $P_L$ as follows:

$$P_L = P_{pulse} * T_{pulse} * F_L \tag{6}$$

An area is polymerized when its local energy is higher than a critical exposure value $E_C$ (mJ/cm²) [2,22] depending on slurry properties. Therefore, dimensions of the final part are known by using the following inequality, applied to the matrix of exposure:

$$E_{total}(x,y,z) > Ec \tag{7}$$

2.3. Light scattering

Nature of material, particle size and shape, powder loading influence laser beam scattering in the photopolymerizable suspension, like laser power and manufacturing parameters (laser velocity, hatch spacing) [12,15,16,23]. This interaction with particles drives the cured area and so the dimensions of the final part. Fig. 3 [14] illustrates the influence of micronic particles in the slurry on the light scattering macroscopic phenomenon, and therefore on laser exposure and cured area. A strong interaction between laser beam and particles induces a reduction of the polymerization depth $Cd$ and an increase in the cure width $Cw$ [3,7,16].

Therefore, we assume here that the scattering is only responsible for the broadening of the gaussian beam shape, considered by the modification of the initial beam radius $W_0$ (11µm) toward a corrected value $W_{0corr}$ via a scattering factor $F_{scatt}$:

$$F_{scatt} = \frac{W_{0corr}}{W_0} \tag{8}$$

Since the scattering phenomenon depends on the manufacturing parameters, $F_{scatt}$ value (and so $W_{0corr}$) will be adjusted thereafter in this paper for each set of variables, in order to take the differences of scattering between these experiments into account.

2.4. Design of experiments

In order to study the influence of laser and manufacturing parameters on dimensions and conversion rates of printed parts, a design of experiments similar to the one used in a previous paper [14] was established with added experiments to widen the range of energies received at the surface of the green part and improve the model accuracy. The laser frequency used for all experiments is 100 kHz, for a layer thickness of 50 µm. A range of different hatches spacing, laser powers and velocities was used, depending on the experiment (Table 1).

**Table 1:** Design of experiments

| **Experiments** | **E1** | **E2** | **E3** | **E4** | **E5** | **E6** | **E7** | **E8** | **E9** | **E10** | **E11** | **E12** |
|---|---|---|---|---|---|---|---|---|---|---|---|---|
| Laser power $\boldsymbol{P_L}$ (mW) | 125 | 125 | 125 | 175 | 175 | 175 | 225 | 225 | 225 | 275 | 275 | 275 |
| Laser velocity $\boldsymbol{V_L}$ (mm/s) | 2500 | 3500 | 4500 | 2500 | 3500 | 4500 | 2500 | 3500 | 4500 | 2500 | 3500 | 2500 |
| Hatch spacing $\boldsymbol{h_S}$ (mm) | 0.02 | 0.03 | 0.04 | 0.03 | 0.04 | 0.02 | 0.04 | 0.02 | 0.03 | 0.02 | 0.02 | 0.03 |

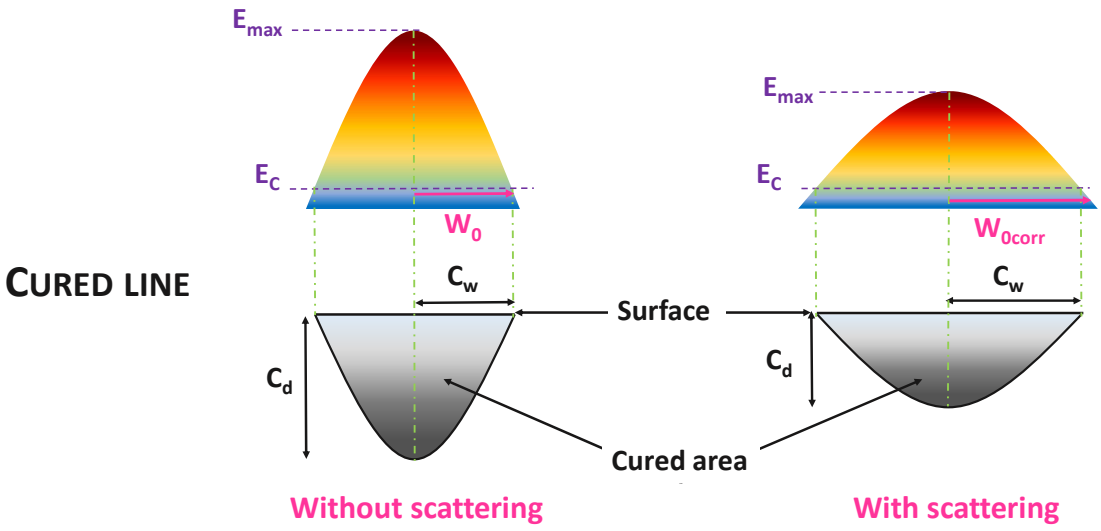


**Fig. 3.** Influence of particles in suspension on the light scattering, exposure distribution and cured area [14]

**3. Photopolymerization modeling**

3.1. Model description

In order to create a map of global exposure $E_{total}$, the domain of simulation is discretized in voxels of the same size in x, y and z directions. The voxel size if defined by the discretization step $p_{dis}$ in the model, as visible in Fig. 1. This step must be at least 5 times smaller than the distance between 2 pulses of the laser source to ensure sufficient accuracy. According to the same operation, a smaller map including only the exposure distribution of a single pulse is obtained thanks to Eq.(4). For this matrix, dimensions in x and y directions are chosen so that the area is large enough to include 99.99% of the total pulse energy. The beam radius of influence $R_L$ allows to determine the pulse matrix dimensions and is defined by [2,14]:

$$R_L = 2.146 * W_0 * F_{scatt} = 2.146 * W_{0corr} \quad (9)$$

The laser radius depends on the scattering phenomenon, therefore it is not the same for each experiment.

This model considers 10 square layers with a thickness of 50µm, resulting in a cubic simulation volume. The laser path for one layer is here defined thanks to laser velocity, hatch spacing and an optional rotation of the lasing direction between layers (Fig. 1). The distance between pulses all along the laser path only depends on the laser frequency and velocity. At each pulse coordinates and for each layer, the small pulse matrix is added into the matrix of global exposure, until the addition of all pulses. Cured areas and final dimensions are then obtained applying the polymerization condition $E > Ec$. The energy distribution in a pulse and the addition of exposures between adjacent pulses are shown in Fig. 4.

The laser acceleration phase is also neglected in this model. Indeed, the optical system is reactive enough to avoid any excessive concentration of pulses at the end of a lasing line that could lead to hot spots. Observations of pulses locations obtained with different laser velocities $V_L$ allowed to estimate this acceleration to at least $10^7\ mm/s^2$. Consideration of this phenomenon in the model only showed a slight difference in the exposure at the very end of the printing area (~100µm), when the laser changes its course. Therefore, we chose here to not take it into account and focus on the inner body that remains the overwhelming majority of the green part.

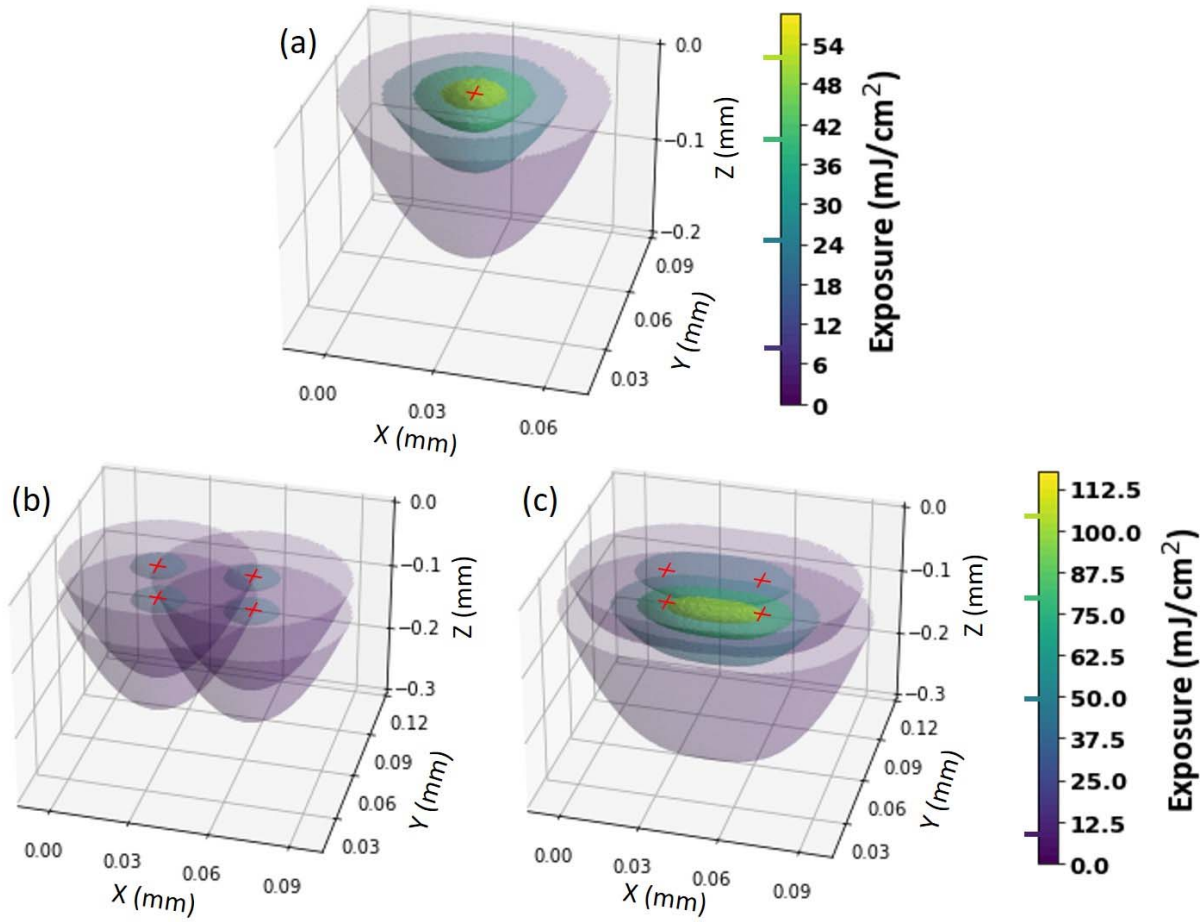


**Fig. 4.** 3D view of laser penetration and exposure for (a) a single pulse, for 2 successive pulses on two different layers (b) before and (c) after addition of each pulse contribution. Displayed surfaces correspond to iso-energy surfaces, with color corresponding to energy of exposure scales. The lowest energy level corresponds to $E_c$ and red crosses to pulse positions.

3.2. Conversion rate simulation

The degree of conversion is the proportion of monomers converted into polymers. In stereolithography process, this conversion rate $p$ depends on the laser intensity I received by the slurry during the whole printing and also kinetic variables linked to the paste composition. The model is defined using a m$^{th}$ order reaction kinetic as a function of three spatial coordinates and time [24]:

$$\frac{\delta p(x,y,z,t)}{\delta t} = r * \left(p_{max} - p(x,y,z,t)\right)^m * I(x,y,z,t)^b \tag{10}$$

$$p(x,y,z,0) = p_0(x,y,z) \tag{11}$$

Where $p_{max}$ is the maximum achievable degree of conversion ($p_{max} \leq 1$) due to the reduction of reactive species mobility upon the curing, $p_0$ is the initial conversion rate at $t = 0$ and b an exponent constant. In order to simplify the simulation model, $p_0$ value is zero, assuming an initial 0% conversion of monomers and the rate constant r is considered temperature independent [24]. This last assumption could induce differences in conversion rate evolution, by not considering the early rise of the reaction rate due to the increasing concentration of radical species during initiation step. We assume this difference to be negligible, since the conversion plateau and gel-point are quickly reached [25]. However, for this model, this choice makes the reaction instant and removes the small time gap between the beginning of laser exposition and the start of conversion rise, reported in literature [5,19,20].

With these previous equations, a time step $\Delta t$ is considered in order to calculate iteratively the increase of conversion rate for each pixel, and during each pulse:

$$p(x,y,z,t+\Delta t) = p(x,y,z,t) + \Delta t * r * \left(p_{max} - p(x,y,z,t)\right)^m * I(x,y,z)^b \tag{12}$$

The value of time step $\Delta t$ must be at least 30 times inferior to the pulse duration to ensure a good accuracy.

3.3. Temperature simulation

Several thermal phenomena must be considered in order to calculate the evolution of temperature during and after printing: i) increase in temperature due to the exothermic polymerization, ii) laser absorption by organic components in the slurry, iii) exchanges by conduction in the part and by convection with air at the surface. In the model, the temperature used for calculation is not absolute, but is the difference between absolute and ambient temperature:

$$\bar{T}(x,y,z,t) = T(x,y,z,t) - T_{amb} \tag{13}$$

The evolution of temperature is then defined in function of this difference of temperatures $\bar{T}$ with the following equations (14) to (17) [10,19,24]:

$$\rho * c_p * \frac{\delta \bar{T}(x,y,z,t)}{\delta t} = \nabla\left(k \nabla \bar{T}(x,y,z,t)\right) + \Delta H * \frac{\delta p(x,y,z,t)}{\delta t} + \varepsilon * I * c_{Abs} \tag{14}$$

Where ρ is the density of the green part, $c_p$ its mass thermal capacity, k the thermal conductivity coefficient and h the heat transfer coefficient. ΔH is referred as the heat of polymerization. Thermal conductivity coefficient, density and thermal capacity are assumed to remain constant all along the reaction of polymerization. In Eq.(14), the first right-hand side term is relative to the conduction, the second one to exothermic heating, and the last one to laser absorption by organic species in the slurry. This last term can be expressed using the penetration depth coefficient $Dp$ and the light intensity only Eq.(2).

The model considers only the air convection at the top surface of the last layer since other surfaces are surrounded by non-cured paste for part sides or for the bottom of the first layer, not in contact with the support. Conduction occurs into each layer, between layers and also between the non-cured paste and part sides. Eq.(15) and Eq.(16) define the thermal exchanges conditions at the edge surfaces of the volume of simulation, with no exchange regarded outside this volume (at $z = L$, $x = x_{min}, x_{max}$ $and$ $y = y_{min}, y_{min}$). Initial temperature inside the volume is the ambient temperature (Eq.(17)). Fig. 5 summarizes all the thermal exchanges occurring in the model, as well as limit conditions at the edges of the simulation volume.

$$k \frac{\delta \bar{T}(x,y,0,t)}{\delta z} = -h * \bar{T}(x,y,0,t) \tag{15}$$

$$\frac{\delta \bar{T}(x,y,L,t)}{\delta z} = \frac{\delta \bar{T}(x_{min},y,z,t)}{\delta z} = \frac{\delta \bar{T}(x_{max},y,z,t)}{\delta z} = \frac{\delta \bar{T}(x,y_{min},z,t)}{\delta z} = \frac{\delta \bar{T}(x,y_{max},z,t)}{\delta z} = 0 \tag{16}$$

$$\bar{T}(x,y,z,0) = 0 \tag{17}$$

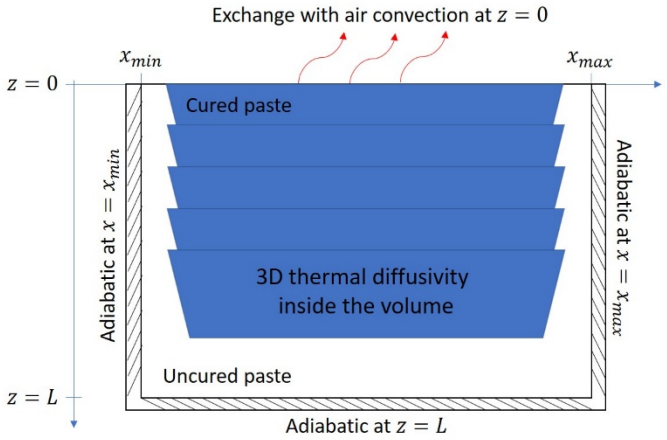


**Fig. 5.** Summary of different thermal exchanges and limit conditions considered in the simulation.

Finally, for the simulation model, the temperature is calculated iteratively using the relation:

$$\bar{T}(t + \Delta t) = \bar{T}(t) + \frac{\Delta t}{\rho * cp} * \left(k * \left(\frac{\delta^2 T}{\delta x^2} + \frac{\delta^2 T}{\delta y^2} + \frac{\delta^2 T}{\delta z^2}\right) + \Delta H * \frac{\delta p}{\delta t} + \frac{I}{ln(10) * Dp}\right) \tag{18}$$

The evolution of temperature is computed during and also between pulses. For this reason, it is necessary to alternate between a low time step $\Delta t$ during pulses and a superior time step $\Delta t^*$ between pulses. Indeed, the duration of a pulse is almost instant (~ns) compared to the time between two pulses (~10 µs). Keeping the same step would make the calculation time too large. This choice is not an issue since the only phenomena considered between pulses are conduction and convection that do not require so much time-accuracy.

3.4. Model fitting

3.4.1. Determination of $Dp$ and $E_c$

In order to determine values of the critical exposure $E_c$ and the penetration depth coefficient $Dp$, the "working curve" (Eq.(19)) [2] allows to link these last parameters with the polymerization depth $Cd$ and the maximum exposure on a lasing line [2]. Because of the lack of dimensional accuracy for a single line and its fragility, the cure width $Cw$ was defined as half of the difference between the experimental and the theoretical width of 30-layer parallelepiped-shape parts. Widths are obtained using a caliper with a precision of ± 5µm. The cure depth $Cd$ is the thickness of a single layer part and is measured with a binocular magnifier, precise to ± 5µm, due to the fragility of single layer parts. To calculate $Cd$ and $Cw$, two samples are printed and three measurements are performed for each experiment and for each sample, respectively. The maximum exposure on a single layer $E_{max1l}$ is taken from the simulation model.

$$Cd = Dp * ln\left(\frac{E_{max1l}}{Ec}\right) \tag{19}$$

From this curve, values of $Dp$ and $E_c$ are extracted using respectively the slope and the intersection point with ordinates. In order to obtain values of $E_{max1l}$ in the model, the use of initial $Dp$, $E_c$ and $W_{0corr}$ values is mandatory. In the Eq.(4), $W_0$ is replaced by $W_{0corr}$ to consider the light scattering. These initial values are taken from J.Tarabeux's work [14] with a similar paste and for a laser frequency of 150 kHz, giving a $Dp$ of 65µm, $E_c$ of 17mJ/cm² and $W_{0corr}$ of 83µm.

For the slurry, final values of $Dp$ and $E_c$ are obtained iteratively, using previously determined values to refine the next ones, according to the process presented in Fig. 6 [14].

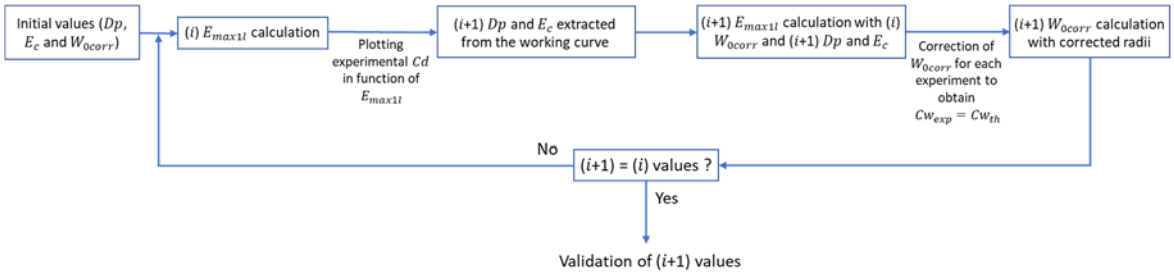


**Fig. 6**. Process for $Dp$ and $E_c$ determination

This process repeats for each iteration until convergence of $Dp$ and $E_c$. Final values are obtained when (i+1) are equal to (i) values to the nearest micron. $Dp$ and $E_c$ only depends on the ceramic-based curable system, and not on the manufacturing parameters, so will keep the same values in all experiments.

3.4.2. A law for $W_{0corr}$ recalculation

Once $Dp$ and $E_c$ are determined for the curable system, a law linking $E_{max1l}$ with $F_{scatt}$ is defined, based on observations of laser scattering [14]:

$$F_{scatt} = \frac{W_{0corr}}{W_0} = a * ln(E_{max1l}) + b \tag{20}$$

Since light scattering depends on the manufacturing parameters, for a given curable system, each experiment has a different adapted beam radius $W_{0corr}$. This adapted $W_{0corr}$ is the value allowing to get simulated cure width $Cw$ equal to the experimental one, and was obtained in the last iteration of the process described in 3.4.1, for each set of parameters. Values of a and b are extracted from the resulting adapted $F_{scatt}$ versus $E_{max1l}$ curve obtained with the mean of corrected radii $W_{0corr}$.

Thanks to this law, for each experiment, a corrected laser radius $W_{0corr}$ can be calculated in a pre-simulation step, based on the maximum exposure on a single layer $E_{max1l}$. This new value of laser radius is then used to simulate a 10-layer part. Obtaining new values of $Dp$, $E_c$ and $W_{0corr}$ is mandatory to make the model representative of the reality, and makes it possible subsequent reliable analysis of dimensions, conversion rate, temperature and homogeneity.

3.4.3. Determination of kinetic variables for conversion rate simulation

In order to determine kinetic variables, conversion rate has been calculated from FTIR spectra obtained on a Nicolet 6700 spectrometer in attenuated total reflection (ATR). Presented results are the average of three measurements realized with 64 scans and a resolution of 2 $cm^{-1}$ on the top of a single layer part. This technique allows to monitor the evolution of carbon-carbon double bonds, and then the conversion rate depending on the manufacturing parameters, since these bonds disappear all along the polymerization. By the comparison of this C=C peak area around 1620 $cm^{-1}$ with a reference peak around 1750 $cm^{-1}$ relative to the carbonyl group which is not influenced by the polymerization, the conversion rate (or degree of conversion) $p$ is defined by [17]:

$$p = \frac{\frac{A_0^{1620}}{A_0^{1750}} - \frac{A_{end}^{1620}}{A_{end}^{1750}}}{\frac{A_0^{1620}}{A_0^{1750}}} \quad (21)$$

Where $A_0$ is the area obtained from the slurry before UV exposure and $A_{end}$ the area measured on cured parts. $A^{1620}$ corresponds to the area under the curve and above the baseline between 1600 and 1650 $cm^{-1}$, and $A^{1750}$ between 1650 and 1780 $cm^{-1}$.

Kinetic parameters are then adapted by trial and error (due to the number of kinetic variables) to lead to a good agreement of the simulation results of conversion with the experimental ones. These simulation results are obtained calculating the average of conversion rate in a relatively large volume defined by the area (∼$mm^2$) and the depth of measurement in FTIR (∼µm), then representatives. In order to define this volume, the simulation model considers the top surface of a 1-layer part, with $x$ and $y$ conditions to ensure that the volume is not close to part edges and thus avoid edge effects. In this way, the simulated volume is as close as possible from the real volume of measurement.

3.4.4. Determination of thermal variables for temperature simulation

Thermal conductivity of both photopolymerizable and cured paste are measured thanks to the hot-disk method. Density and thermal capacity of the mixture are recalculated using values for pure resin and alumina [19,24]. This theoretical density has been confirmed by measurement on a cured part.

In order to estimate the polymerization heat, temperature increases are measured during curing of a 5x3cm surface thanks to an IR-camera. Targeting the last printed lines, the maximum temperature is obtained for each set of parameters, with 3 measures per experiment. Several polymerization heats are then used in the model to obtain the same temperature differences than measured ones. It is important to note that the resulting polymerization heat may be under-estimated because of the limited volume of simulation inducing a smaller time for the temperature to decrease between two adjacent lasing lines, and thus a higher temperature in the model than in manufactured parts. We tried to reduce this difference by increasing the volume of simulation, but further improvements would need way more memory for simulation.

3.5. Homogeneity analysis

In order to quantify the influence of manufacturing parameters on the homogeneity of printed parts and potentially optimize subsequent mechanical properties by reducing internal stresses, the simulation computes the MAD factor, measuring the absolute distance of values around the median [26]:

$$\forall\, Ek > Ec : MAD = \frac{1}{n}\sum_{k=1}^{n} |E_k - E_{median}| \quad (22)$$

This model only considers voxels (and the associated exposure) inside a sphere at the center of the printed part, for which the exposure $E_k$ is strictly superior to the critical exposure $E_c$. In doing so, side effects are not considered and the results characterize the inner body. $E_{median}$ is the median exposure among all pixels inside the sphere, numbered n. Thanks to MAD, a new factor can be studied for relative deviation around the median (MRD), defined as follows and similar to a coefficient of variation:

$$MRD\ (\%) = \frac{MAD}{E_{median}} * 100 \quad (23)$$

These factors allow to study various parameters which influence the homogeneity of green parts, like laser velocity, hatch spacing, layer thickness or even the rotation of lasing angle between layers.

**4. Results and discussion**

4.1. Dimensions of green parts

Experimental results for cure depths and cure width are presented in Fig. 7. Influences of laser power, velocity and hatch spacing on cure dimensions have been already studied and will not be the subject of this paper [14]. However, this work confirms previous results: increasing laser power or decreasing laser velocity and hatch spacing allow to get a more significant curing.

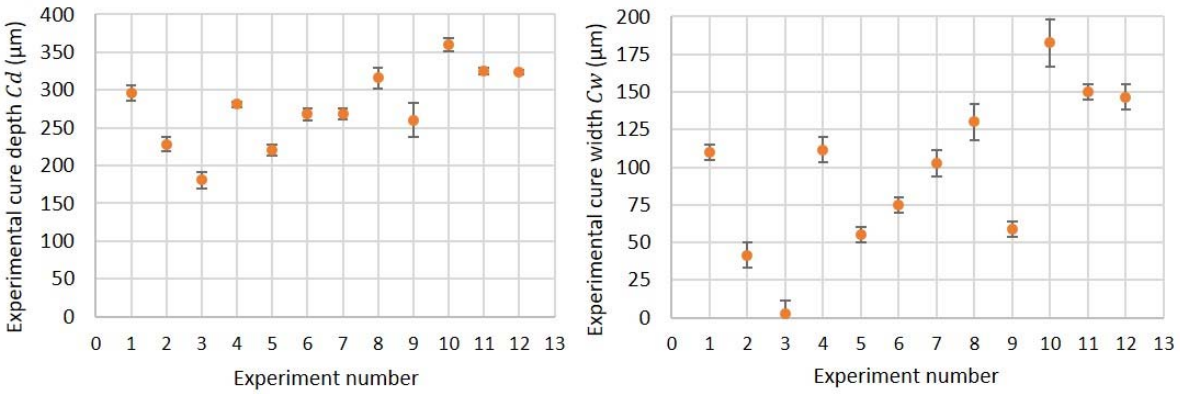


**Fig. 7.** Average Cure depths $Cd$ and cure widths $Cw$ measured for each experiment.

4.2. Identification of critical exposure $E_c$ and penetration depth coefficient $Dp$

Since initial parameters were already identified for similar paste and laser [14], final values are quickly obtained after 2 iterations according to the method described in 3.4.1. The last working curve given in Fig. 8 allows to determine $Dp = 87\ \mu m$ and $Ec = 9\ mJ/cm^2$, for an average corrected radius of 80 µm, very close to the initial one (i.e. 83 µm). Modification of laser frequency, as well as more precise dimensional measurements in this work could explain differences between new and previous values of $Dp$ (65µm) and $Ec$ (17 mJ/cm²) [14].

These values are quite far from those reported by Jacobs for an unloaded resin: $E_{c\ unloaded} = 5{,}6\ mJ/cm^2$, $Dp_{unloaded} = 178\ \mu m$ and $W_0 = 11\ \mu m$ [2]. The presence of ceramic particles in slurry seems to be responsible for the large increase in corrected laser radius and reduction of $Dp$.

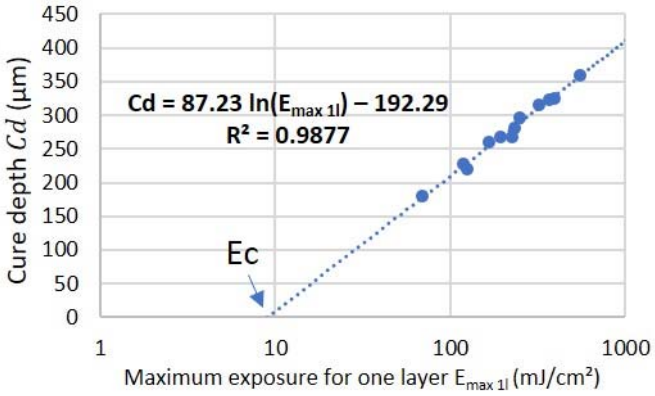


**Fig. 8.** Last working curve used for parameters identification.

4.3. Determination of a and b values for $W_{0corr}$ recalculation

According to the process described in 3.4.2 , previously determined values of $Dp$ and $E_c$ are used in order to adapt simulated to experimental widths. Adapted values of $F_{scatt}$ are then obtained. Starting from the average adapted radius $W_{0corr}$ (80 µm), values of maximum exposure for one layer $E_{max1l}$ are simulated and plotted in function of the adapted scattering factor (Fig. 9). This curve allows to determine coefficients $a = 6.46$ and $b = -27.47$. The slope value points out a huge dependency of scattering phenomenon on the energy density, determined by manufacturing parameters and laser power, as already reported [5,14,20,27].

It is now possible to recalculate corrected laser radii, in function of the maximum exposure obtained during the lasing of a single layer.

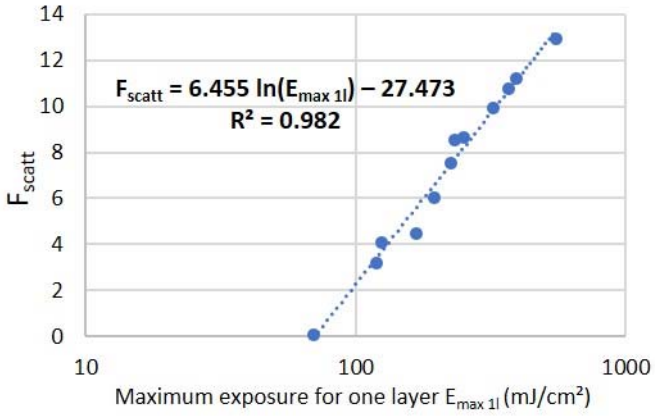


**Fig. 9.** Dependency between maximum exposure on a single layer and scattering factor $F_{scatt}$

4.4. Limits of the simulation model

The very low value of $F_{scatt}$, lower than 1, needed for E3 (i.e. $F_{scatt} = 0.09$ for $E_{\max 1l} = 70\ mJ/cm^2$) to make the simulated cure width fit with the experimental one accounts for the limit of the model. This model does not take into account all physical phenomena occurring during the polymerization process, like shrinkage, species mobility, oxygen inhibition at the surface, refraction at polymer/slurry interface or physical properties transformation [20], but just considers the cured area dependency on the energy received during lasing. For example, experimental dimensions used to make simulated dimensions fit in the model are measured on greens parts, then after shrinkage due to polymerization. The shrinkage is then included, in this model, via the correction of the laser radius. A more efficient model could consider a slightly superior $W_{0corr}$ and subsequently reduce the matrix size depending on the shrinkage factor for each direction. This would require to separate the influence of scattering (increasing part widths) and the one of shrinkage (decreasing part dimensions) on measured part sizes.

The low calculated value of $W_{0corr}$ obtained for E3 corresponds to a corrected beam radius lower than $W_0$ , and to a very thin and deep exposed volume which does not overlap between pulses. This situation cannot lead to a single cohesive part. However, under E3 parameters, the part was successfully constructed and can be easily manipulated. This suggests that our model applied to our curable ceramic-based system is not reliable for low exposures, leading to a scattering factor $F_{scatt} < 1$. Future versions of the model could solve this issue by including shrinkage and other physical phenomena listed before.

4.5. Comparison between numerical and experimental results

Thanks to all previously determined parameters, the simulation is performed. Fig. 10 shows both values of experimental and simulated cure depths $Cd$ and cure widths $Cw$. Except for E3 for which the simulation is not reliable, the numerical values are very close to experimental dimensions. Therefore, this simulation model makes it possible to predict the influence of the energy density on cured dimensions. Fig. 11 represents the energy distribution on a cross-section of the part simulated with E2 parameters, as well as a 3D visualization of the part shape. This highlights the existence of tiny “sawtooth” on the part edges, explained by laser scattering and energy reduction with depth. The bulk of the printed part presents exposure heterogeneity in a single layer but also between layers. Indeed, bottom layers receive more energy than top layers. Because of the high laser penetration depth, larger than a layer thickness, each layer receives a part of the beam energy from the exposure of subsequent layers. This result has already been reported through conversion rate measurements [17].

The homogeneity in a single layer can be improved by the reduction of the layer thickness, which is detrimental to the fabrication time. This also plays a role in the optimization of post-sintering mechanical properties [28].

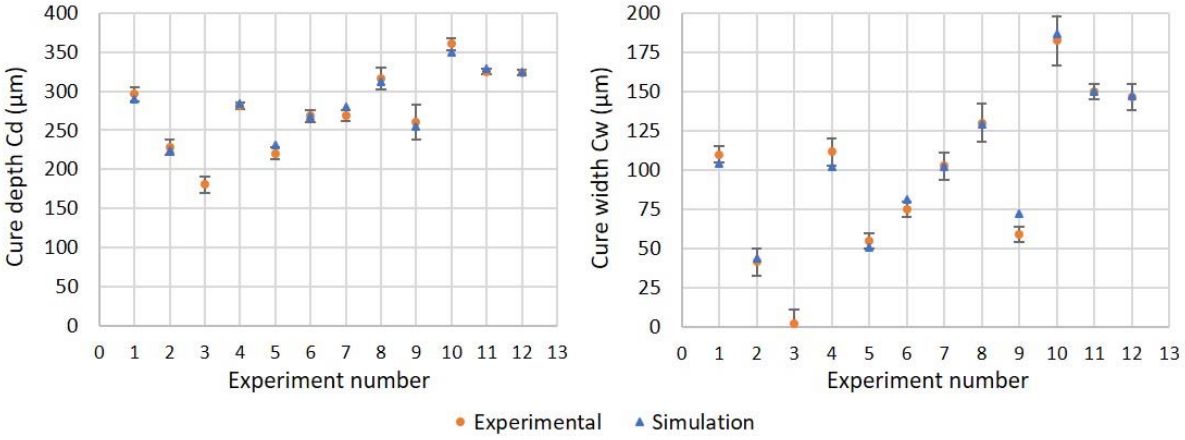


**Fig. 10.** Comparison between experimental and simulated cure depths $Cd$ and cure widths $Cw$

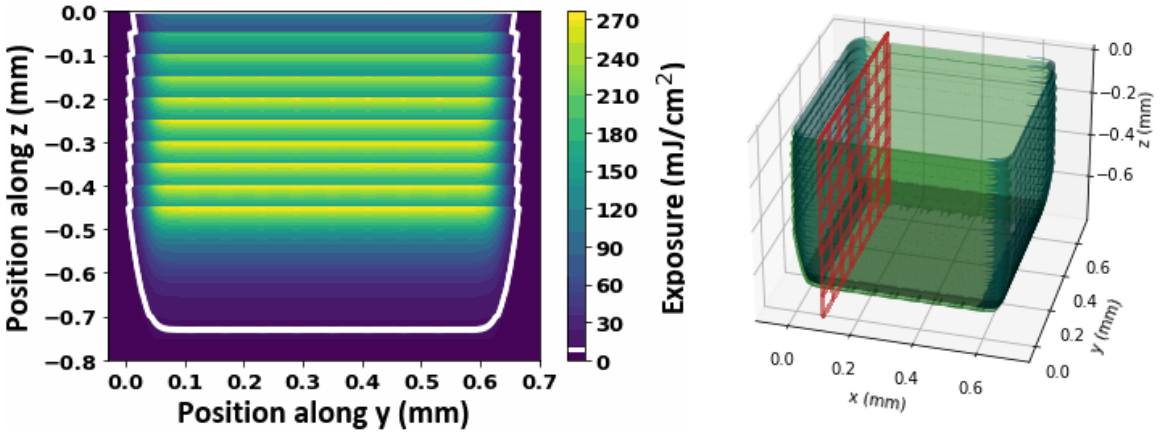


**Fig. 11.** Exposure on a cross section of the printed part ($x = 0.1\ mm$) and 3D visualization of the corresponding cross-section position (in red). These results are obtained with E2 parameters. White line (on the left) and green surfaces (on the right) refer to piece edges and are defined using $E > Ec$.

4.6. Conversion rate calculation

Comparison between numerical and experimental conversion rates (or degrees of conversion) allowed to determine kinetic values for our paste: $r = 5 * 10^{-3}\ s^2\ kg^{-1}$, $pmax = 0.63$, $b = 1$ and $m = 3$ (Eq.(10)). Very close conversion rates are obtained using these values in the model (Fig. 12). Although intuitive, higher conversion rates seem to be achieved applying a higher exposure during printing, as already stated [9,17]. For exposures that are already high enough, continuing to increase it does not lead to a large increase in the conversion rate.

As well as the reduction of species mobility due to the gelling of the organic phase, this can be explained thanks to the scattering factor. Indeed, a large exposure leads to a wide scattering, thus, keep rising the exposure by a $f$ factor will result in a significant increase of the scattering surface by a factor $f' > f$. A slightly higher energy is then distributed over a much wider area, which results in lowering the maximum exposure in a single pulse and increasing the cure width, as presented in Fig. 13. Having a too large scattering factor (or corrected laser radius) may cause resolution issues on the final part. To associate a good dimensional accuracy and a sufficient conversion rate, it seems preferable to select a mid-range exposure value (~250 mJ/cm² on a single layer), also allowing to avoid too large "sawtooth" on piece edges.

The simulation of a 10-layer part is then performed thanks to previously determined kinetic variables, and the evolution of the maximum conversion rate in function of both the time of printing and the depth is studied (Fig. 14). As expected, due to laser penetration ($Dp$) corresponding to several layer thicknesses (50 µm thick layers), the conversion rate is notably influenced by the exposure up to about 5 subsequent layers. This number of layers also depends on the scattering factor, since it drives the penetration depth. Scattering also plays a role in the difference of conversion rate between the top and the bottom of a layer, which can induce residual stresses due to the associated polymerization shrinkage. This difference could be reduced by decreasing the layer thickness, at the cost of a higher number of layers needed. As well as improving the exposure homogeneity, this could lead to a better average conversion rate in the whole part. Lowering the exposure can also decrease these conversion differences in a layer.

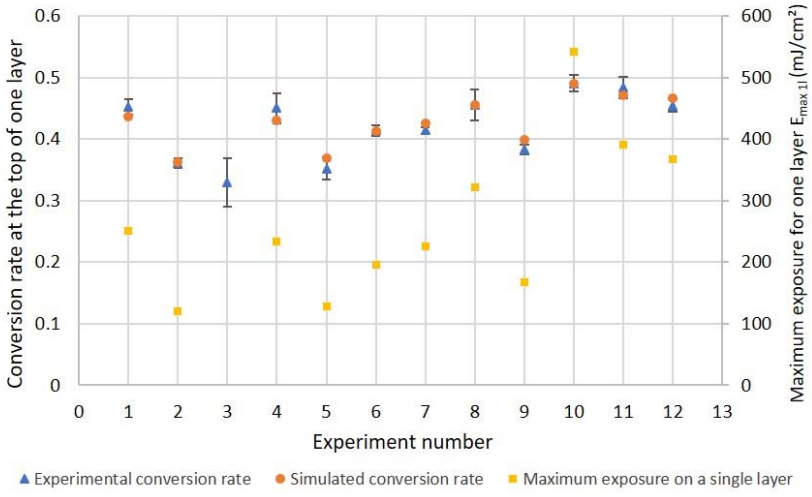


**Fig. 12.** Simulated and experimental conversion rates at the top of a single layer part, compared to the maximum exposure received, for each set of parameters.

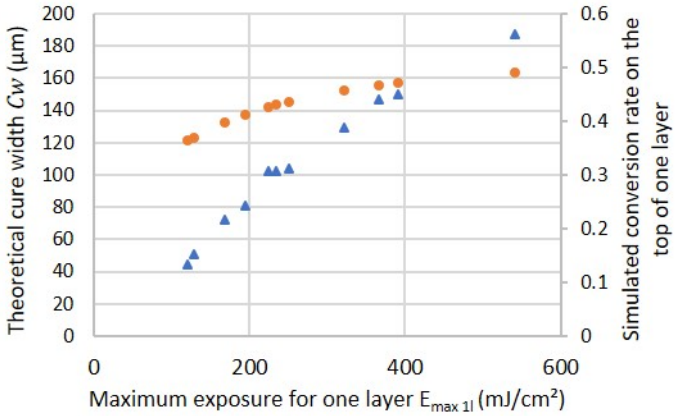


**Fig. 13.** Theoretical cure widths (blue triangles, left) and simulated conversion rates (orange circles, right) in function of the overall maximum exposure on one layer, for each set of parameters except E3.

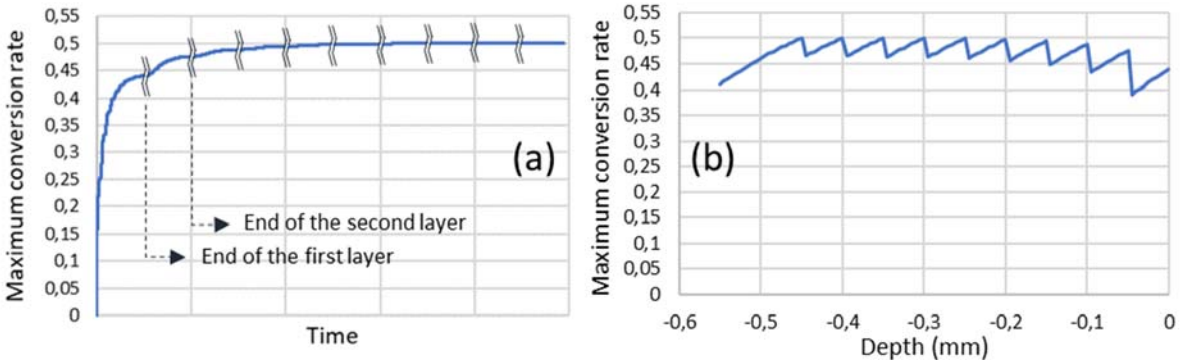


**Fig. 14.** Evolution of the maximum conversion rate in function of (a) the time of printing and (b) the depth, on a 10-layer part manufactured with E1 parameters. The depth 0mm corresponds to the top surface of the part. Time is not displayed because of discontinuity between layers due to stereolithography process. Transition from one layer to another (~30s) is here considered instant to help observation.

4.7. Temperature calculation

According to processes described in 3.4.4, material properties are listed in Table 2. In addition to mixture thermal capacity and density, the green part conductivity $k_{part}$ only was also considered since the polymerization is fast enough to reach this level of conversion during laser exposure. Temperature increases, between 4 and 10°C, have been measured by IR during insolation, according to manufacturing parameters. These values are used to determine the polymerization heat $\Delta H$. For a pure resin without alumina particles, the temperature increase was much higher and can reach up to 50°C. This difference may be due to the polymerization heat, lowered in the loaded system by the presence of alumina particles. Indeed, a rather low value of $\Delta H$ is obtained. For comparison, a pure HEMA (2-hydroxyethyl methacrylate) monomer [10] presents a polymerization heat of about 400 $kJ/kg$, against 10.7 $kJ/kg$ for our system (17.6 wt% organic compounds). Considering the low temperature increase and potential reduction due to the limited volume of simulation (3.4.4), this low value of $\Delta H$ seem acceptable. The maximum temperature also highly depends on polymerization kinetics, and is logically different according to the curable system used. The presence of high conductivity alumina particles, with respect to the organic phase, may also be responsible for a quicker temperature decrease.

**Table 2:** Material properties used for simulation.

| Parameter | Value | Unit | Description |
|---|---|---|---|
| $\rho_{Al}$ | 3900 | $kg/m^3$ | Alumina density [19,24] |
| $\rho_{resin}$ | 1150 | $kg/m^3$ | Resin density [19,24] |
| $\rho_{mixt}$ | 2800 | $kg/m^3$ | Mixture density (58% vol. charge) (Measured) |
| $c_{p\ Al}$ | 900 | $J/(kg.K)$ | Alumina thermal capacity [19,24] |
| $c_{p\ resin}$ | 1700 | $J/(kg.K)$ | Resin thermal capacity [19,24] |
| $c_{p\ mixture}$ | 1040 | $J/(kg.K)$ | Mixture thermal capacity (Calculated) |
| $h$ | 10 | $W/(m^2.K)$ | Heat transfer coefficient [16,24] |
| $k_{paste}$ | 1.63 | $W/(m.K)$ | Photopolymerizable paste conductivity (Measured) |
| $k_{part}$ | 2.29 | $W/(m.K)$ | Cured part conductivity (Measured) |
| $\Delta H$ | $3.10^7$ | $J/m^3$ | Polymerization heat (Calculated) |

Simulation is then performed with previous parameters to compute the evolution of temperature inside a part, during insolation. For memory issues, a smaller volume must be considered to allow the simulation to run properly with 4 dimensions. For this reason, the simulation integrates 2 layers, in order to study at least the temperature behavior at the interface between 2 layers. The laser path and pulses are displayed on Fig. 15, and are repeated for each layer. The ambient temperature is set at 20°C.

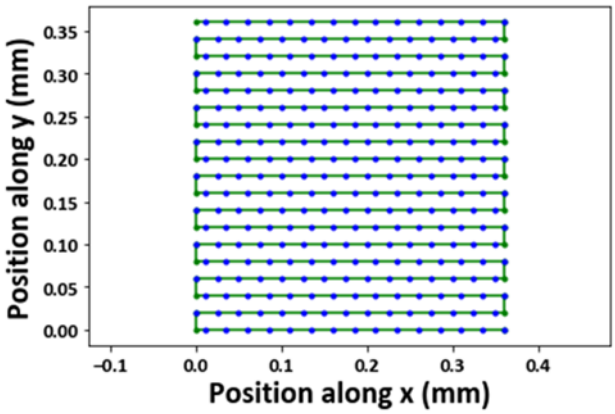


**Fig. 15.** Laser path (green line) and pulses (blue dots) applied on a single layer, for E1 parameters.

Fig. 16 illustrates, for E1 parameters, both the variation of temperature inside a part during printing of a layer and the maximum temperature in function of the time. Thermal exchange caused by diffusivity seems faster than exchange from convection at the surface of the part. Indeed, before coming back to ambient temperature, the internal temperature balances quickly via diffusivity. This quick thermal exchange is followed by a longer-term exchange, compared to diffusivity, with the air convection at the top surface allowing to cool down the part. The diffusivity effect is also visible on Fig. 17(e-f), where lost energy from the surface allowed to warm up the bottom.

Temperature variations being responsible for material expansion and contraction, a non-uniform thermal field will result in stresses in the body [29]. Temperature can also influence the polymerization, in particular via the viscosity of the organic phase and the mobility of the reactive species. As visible on Fig. 17(f), a difference of about 4°C is visible between the top and the bottom of the last layer (50µm). This difference, although low, leads to a non-uniform cooling. According to kinetics and heat of the polymerization reaction, this phenomenon may induce large temperature differences in bulk. A temperature gradient also exists in x and y directions, and mainly depends on light scattering intensity, as illustrated in Fig. 3. For weak scattering, the laser beam radius $W_{0corr}$ remains low, therefore the insolated area is thin and deep, resulting in high temperature gradients in these directions. In stereolithography process, this temperature gradient is inevitable, thus, being able to predict and reduce temperature differences in body may likely have an impact on final mechanical properties.

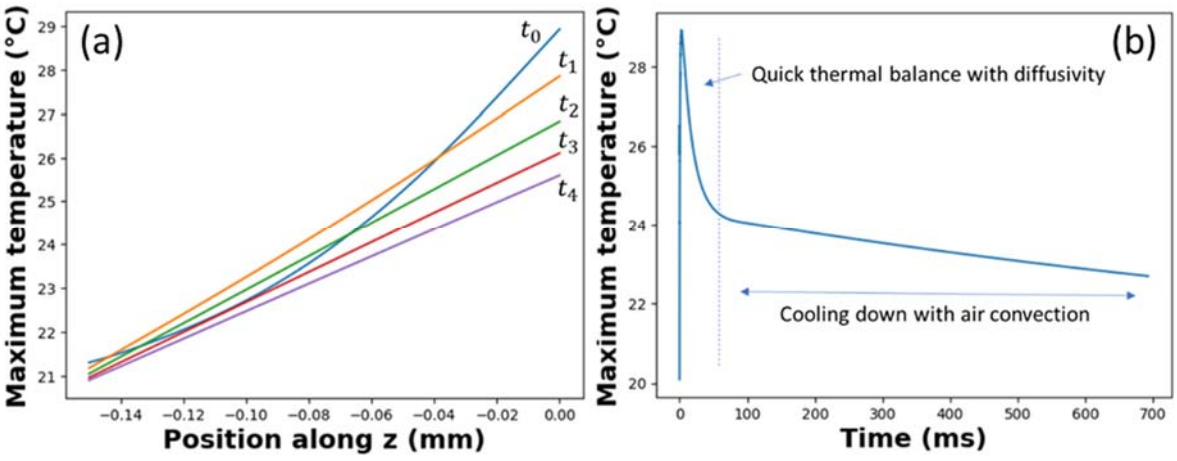


**Fig. 16.** Evolution of the maximum internal temperature (a) after the last pulse, in function of the depth and for different times ($t_0$-$t_4$) and (b) in the whole part, in function of the time during and after laser exposure. In the left graph, each curve is separated by about 3ms, and $t_0$ corresponds to the moment the last pulse ends.

It is important to note the existence of a temperature slope discontinuity between 2 layers during printing. Indeed, bottom layers are already polymerized, and consequently their conversion rates will not increase as much as the top one. This difference of conversion rate increase induces differences of temperature after the end of each pulse, before the diffusivity effect was able to balance temperature between layers. Despite the quick diffusivity phenomenon, this difference can be observed on Fig. 17(d-e), and especially on Fig. 18, above and below the interface (red dotted line), and, coupled with conversion rate discontinuity, may be responsible for stress issues during mechanical load.

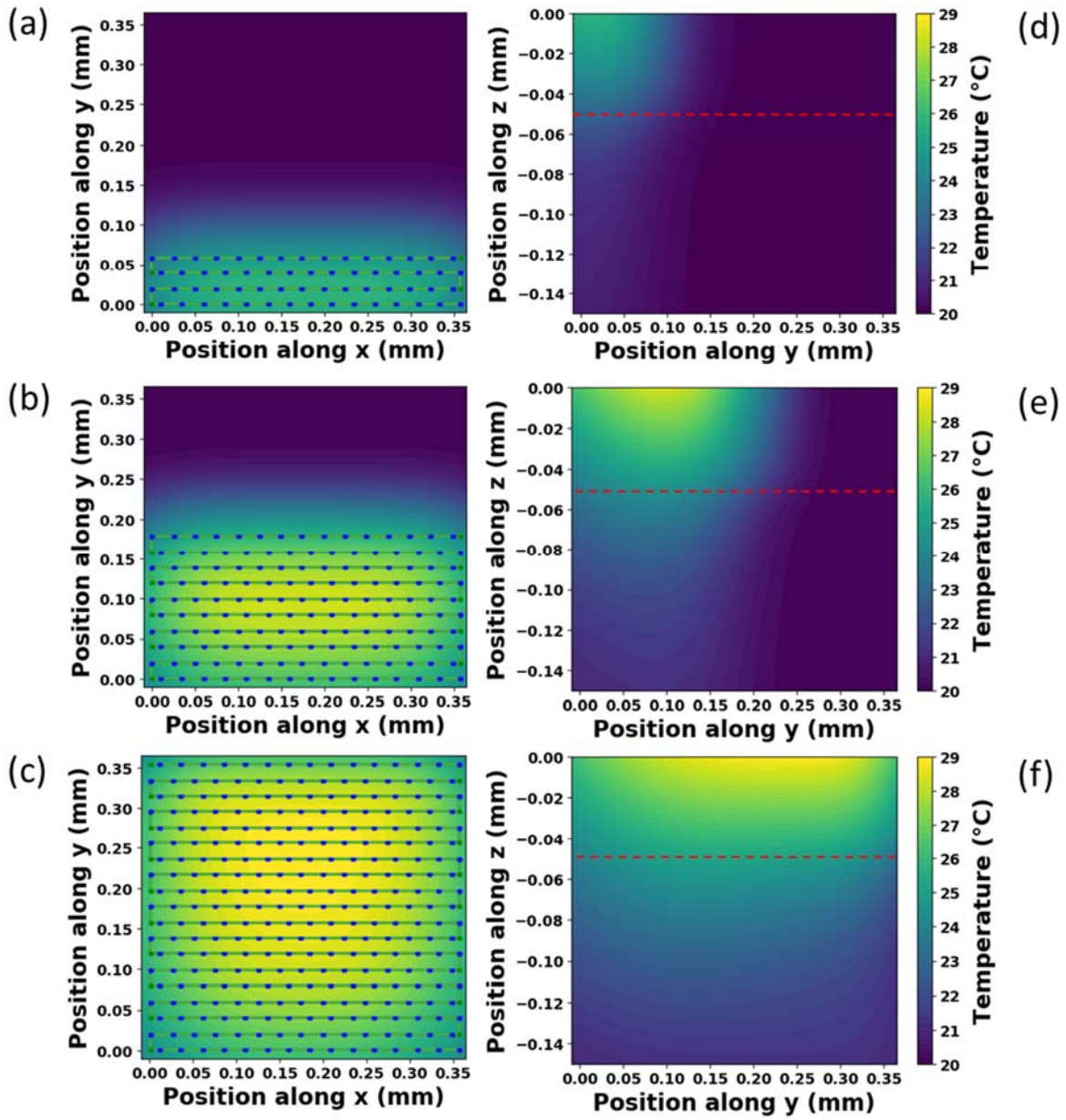


**Fig. 17.** Temperature simulation in a 2 layer-part printed with E1 parameters: (a-c) Top view at $z = 0\ mm$ and (d-f) cross section at $x = 0.18\ mm$. The data are taken at three different times: (a,d) after 4 lasing lines, (b,e) after 10 lasing lines and (c,f) after the last line. Pulses positions correspond to blue dots on top view. The red dotted lines correspond to the interface between the second layer (ongoing, at the top) and the first one (already polymerized, at the bottom).

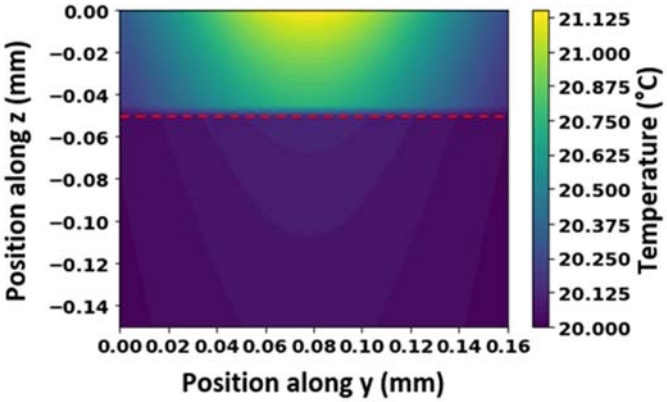


**Fig. 18.** Temperature discontinuity at the interface between 2 layers at the end of a single pulse. This pulse targets the top surface of a 2 layer-part printed with E1 parameters. The bottom layer (under the red dotted line) is already insolated and polymerized, while the top layer receives its first pulse.

4.8. Homogeneity quantification

Homogeneity factors MAD and MRD were calculated for each set of parameters of the design of experiments. Fig. 19 shows MAD in function of the median exposure into the inner sphere of the part. All experiments have the same MRD value, resulting in a linear curve with a slope value equal to MRD ($= 15.88\,\%$). This MRD value does not seem further improvable by only modifying hatch spacing or laser velocity, as stated in Fig. 20. In the range of parameters of this design of experiments, pulses are close enough to avoid large energy gaps that could lead to another source of inhomogeneity in the bulk. For a laser frequency of 100 kHz and a velocity of 3000mm/s, the distance between two pulses along the laser displacement is 30µm, which is very close to hatch spacing values used for experiments. Indeed, under a critical distance between pulses (in x or y direction), modifications of laser velocity or hatch spacing influence the overall exposure, so the conversion rate and the cure width of green parts. The best position on this stationary part of the curve is then a compromise between a better conversion rate and a better printing resolution. A too large exposure could also lead to curling issues, due to the more important polymerization shrinkage or the non-uniform thermal cooling effect [30,31].

It is important to note that these critical values depend on the paste used for the experiment. Consequently, optimal parameters may be different depending on the curable system. This simulation just highlights the existence of an optimum (at the right of the stationary part) to ensure the best resolution without any sacrifice on the homogeneity.

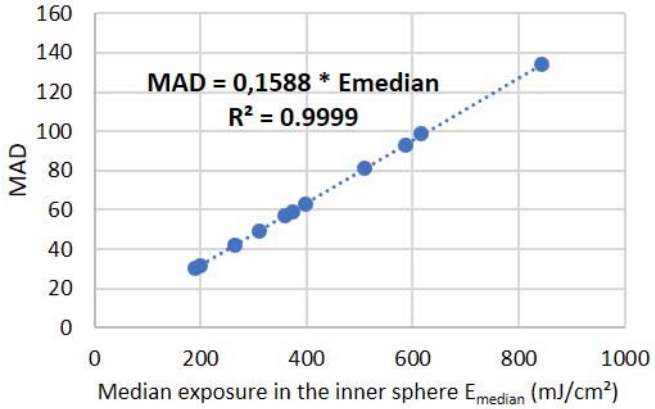


**Fig. 19.** MAD factor in function of the median exposure in the inner sphere of a 10-layer part, for each set of parameters except E3.

This homogeneity study has also been performed in function of the rotation of lasing angle between layers, and does not have reported any notable difference in MAD and MRD (<0.1% of variation), compared to same parameters without rotation. Modification of lasing angle does not seem to have any influence on the homogeneity. In the same way, considering that scattering phenomenon is not affected by laser frequency, its variation did not show any homogeneity difference, except for low frequencies (<30kHz) for which the distance between pulses becomes too large and induces energy gaps.

Besides, layer thickness has a strong impact on the homogeneity, as presented in Fig. 21. Decreasing this distance between two layers allows to improve the homogeneity, as well as the conversion rate, since the average exposure is higher. Consequently, the choice of a relatively small layer thickness may have a huge impact on mechanical properties of green parts, and subsequently of post-sintering pieces. On the other hand, a too low layer thickness will result in a slightly worse resolution and potentially large deformations of the printed part, because of the high exposure reached.

In order to reach a good resolution, homogeneity and conversion rate, it seems relevant to consider a small layer thickness associated with a small energy density on one layer, with a set of manufacturing parameters allowing to remain on the stationary part of MRD curves in Fig. 20. This choice seems to be the best compromise to obtain a good homogeneity (low MRD) without reaching too high values of cure widths and exposure that could cause deformations. Moreover, since the printing time is long enough for the slurry to cool down between two layers (~30s), smaller exposures per layer and thinner layers allow to reach high conversion rates avoiding high temperatures deformation issues.

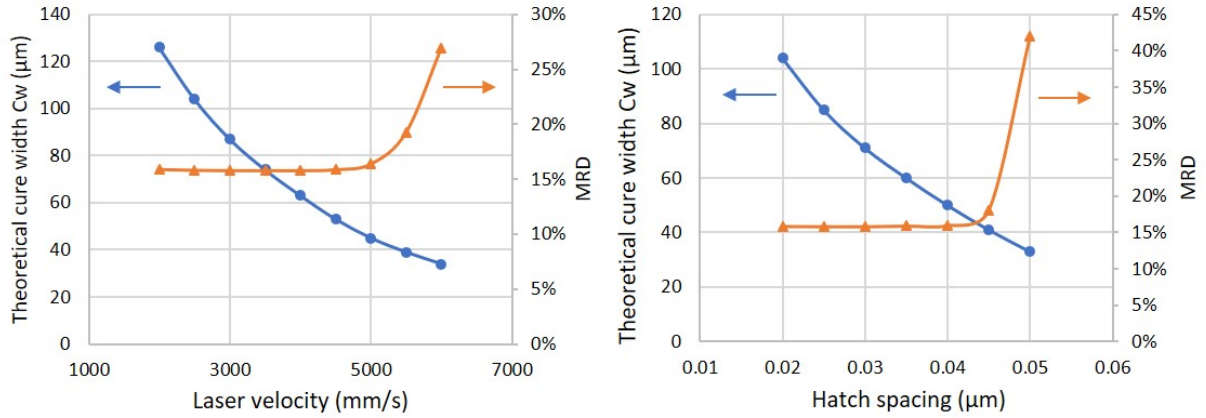


**Fig. 20.** Evolution of MRD (orange, right) and theoretical cure width $Cw$ (blue, left) in function of (a) the laser velocity and (b) hatch spacing. Fixed parameters (laser power, and respectively (a) hatch spacing and (b) laser velocity) are taken from E1 experiment.

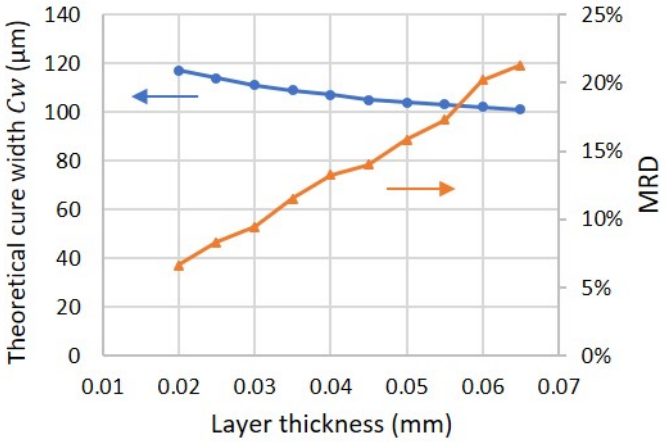


**Fig. 21.** Evolution of MRD (orange, right) and theoretical cure width $Cw$ (blue, left) in function of the layer thickness. Fixed parameters (laser power, hatch spacing and laser velocity) are taken from E1 experiment.

**5. Conclusions and perspectives**

Thanks to the 3D simulation model of photopolymerization developed, the influence of various manufacturing parameters on laser scattering, part dimensions, conversion rate and its homogeneity, and temperature gradient generated during printing has been evaluated. First, in order to quantify the scattering intensity, a law adapted to the ceramic-based curable system used, has been established. This law defines, with a good precision, a corrected laser radius in function of the energy density on one layer, depending on manufacturing parameters (hatch spacing, laser power and velocity). Then, according to the pulsed laser used, the exposure of a single laser pulse was defined in three dimensions. The energy received from one pulse allowed to calculate both the 3D matrix of exposure of the part and the degree of polymerization at each point. Temperature elevation during printing was calculated considering the evolution of the conversion rate.

This model showed a really good ability to predict curing dimensions and conversion rates, but needs the material-related values ($E_c$, $Dp$, kinetic, thermal and scattering law constants) which are specific to each curable suspension. Although adequate for the present studies, this model could be improved to consider complex-shape patterns. The model has shown not to be reliable for low exposures, leading to a scattering correcting factor ($F_{scatt}$) lower than 1. Future versions of the model could solve this issue by including shrinkage and other physical phenomena such as oxygen inhibition at the surface, refraction at polymer/slurry interfaces or physical properties variations. Additionally, applying the same energy but over one or several scans may have an impact on dimensions, conversion rates and homogeneity. Even though needing another design of experiment to compare with, considering this number of laser scans per layer could bring interesting information about the polymerization kinetics.

The prediction of the temperature variation during stereolithography process is of prime importance because it may likely have an impact on final mechanical properties. Heat of the polymerization reaction and laser absorption by organic species are leading to a non-uniform

thermal field, according to thermal exchanges ability of the curable system and the part geometry (diffusivity, convection at the surface) and are responsible for stresses in the body. In this respect, temperature and homogeneity analysis provided answers to optimize green part dimensions and accuracy, to limit residual stresses and potentially improve post-sintering mechanical properties. Using a low exposure associated with thin layers, certainly at the expense of the manufacturing time, allows to improve the resolution and the homogeneity of conversion in the bulk, as well as avoiding large temperature increases. Present results did not show large temperature increases due to polymerization, then the impact on mechanical properties is expected to be negligible. However, this process applied to a highly reactive system with fast polymerization kinetics would allow to estimate the temperature profile for highly exothermic curing, much more willing to cause mechanical stress.

To confirm previous assumptions about homogeneity, a mechanical study will be performed to highlight the influence of manufacturing parameters on green part mechanical properties, and even on sintered ones. Considering both conversion rate and temperature gradients provided by this model seems relevant in order to improve predictions of green part deformations.

**Acknowledgements**

This study was supported by the region Nouvelle-Aquitaine, France.

**References**

[1] M.L. Griffith, J.W. Halloran, Freeform Fabrication of Ceramics via Stereolithography, J. Am. Ceram. Soc. 79 (1996) 2601–2608. https://doi.org/10.1111/j.1151-2916.1996.tb09022.x.
[2] P.F. Jacobs, Rapid Prototyping & Manufacturing: Fundamentals of Stereolithography, Chapter 4: Fundamental Processes, Society of Manufacturing Engineers, 1992.
[3] G.A. Brady, T.-M. Chu, J.W. Halloran, Curing Behavior of Ceramic Resin for Stereolithography, (1996) 403–410.
[4] T. Chartier, Additive Manufacturing to Produce Complex 3D Ceramic Parts, J. Ceram. Sci. Tech. (2014) 95–104. https://doi.org/10.4416/JCST2014-00040.
[5] J.W. Halloran, Ceramic Stereolithography: Additive Manufacturing for Ceramics by Photopolymerization, Annu. Rev. Mater. Res. 46 (2016) 19–40. https://doi.org/10.1146/annurev-matsci-070115-031841.
[6] J. Deckers, Additive Manufacturing of Ceramics: A Review, J. Ceram. Sci. Tech. (2014). https://doi.org/10.4416/JCST2014-00032.
[7] S. Zakeri, M. Vippola, E. Levänen, A comprehensive review of the photopolymerization of ceramic resins used in stereolithography, Addit. Manuf. 35 (2020) 101177. https://doi.org/10.1016/j.addma.2020.101177.
[8] H. Algamaiah, N. Silikas, D.C. Watts, Conversion kinetics of rapid photo-polymerized resin composites, Dent. Mater. 36 (2020) 1266–1274. https://doi.org/10.1016/j.dental.2020.07.008.
[9] Y. Gao, L. Xu, Y. Zhao, Z. You, Q. Guan, 3D printing preview for stereo-lithography based on photopolymerization kinetic models, Bioact. Mater. 5 (2020) 798–807. https://doi.org/10.1016/j.bioactmat.2020.05.006.
[10] M.D. Goodner, C.N. Bowman, Development of a comprehensive free radical photopolymerization model incorporating heat and mass transfer effects in thick films, Chem. Eng. Sci. (2002) 14.
[11] C. Sun, X. Zhang, Experimental and numerical investigations on microstereolithography of ceramics, J. Appl. Phys. 92 (2002) 4796–4802. https://doi.org/10.1063/1.1503410.
[12] S.P. Gentry, J.W. Halloran, Light scattering in absorbing ceramic suspensions: Effect on the width and depth of photopolymerized features, J. Eur. Ceram. Soc. 35 (2015) 1895–1904. https://doi.org/10.1016/j.jeurceramsoc.2014.12.006.
[13] D.T. Pham, R.S. Gault, A comparison of rapid prototyping technologies, Int. J. Mach. Tools Manuf. 38 (1998) 1257–1287. https://doi.org/10.1016/S0890-6955(97)00137-5.
[14] J. Tarabeux, V. Pateloup, P. Michaud, T. Chartier, Development of a numerical simulation model for predicting the curing of ceramic systems in the stereolithography process, J. Eur. Ceram. Soc. 38 (2018) 4089–4098. https://doi.org/10.1016/j.jeurceramsoc.2018.03.052.
[15] S.P. Gentry, Factors Affecting the Resolution of Photopolymerized Ceramics, Thesis, 2012.
[16] S. Westbeek, J.J.C. Remmers, J.A.W. van Dommelen, M.G.D. Geers, Multi-scale process simulation for additive manufacturing through particle filled vat photopolymerization, Comput. Mater. Sci. 180 (2020) 109647. https://doi.org/10.1016/j.commatsci.2020.109647.
[17] T. Chartier, C. Dupas, P.-M. Geffroy, V. Pateloup, M. Colas, J. Cornette, S. Guillemet-Fritsch, Influence of irradiation parameters on the polymerization of ceramic reactive suspensions for stereolithography, J. Eur. Ceram. Soc. 37 (2017) 4431–4436. https://doi.org/10.1016/j.jeurceramsoc.2017.05.050.
[18] G. Gouesbet, G. Gréhan, Diffusion des faisceaux laser par des particules, (1998) 23.
[19] S. Westbeek, J.A.W. van Dommelen, J.J.C. Remmers, M.G.D. Geers, Multiphysical modeling of the photopolymerization process for additive manufacturing of ceramics, Eur. J. Mech. - ASolids. 71 (2018) 210–223. https://doi.org/10.1016/j.euromechsol.2018.03.020.
[20] T. Hafkamp, G. van Baars, B. de Jager, P. Etman, A feasibility study on process monitoring and control in vat photopolymerization of ceramics, Mechatronics. 56 (2018) 220–241. https://doi.org/10.1016/j.mechatronics.2018.02.006.
[21] X. Li, K. Hu, Z. Lu, Effect of light attenuation on polymerization of ceramic suspensions for stereolithography, J. Eur. Ceram. Soc. 39 (2019) 2503–2509. https://doi.org/10.1016/j.jeurceramsoc.2019.01.002.
[22] Y. Abouliatim, T. Chartier, P. Abelard, C. Chaput, C. Delage, Optical characterization of stereolithography alumina suspensions using the Kubelka–Munk model, J. Eur. Ceram. Soc. 29 (2009) 919–924. https://doi.org/10.1016/j.jeurceramsoc.2008.07.008.
[23] S. Westbeek, J.A.W. van Dommelen, J.J.C. Remmers, M.G.D. Geers, Influence of particle shape in the additive manufacturing process for ceramics, Comput. Math. Appl. 78 (2019) 2360–2376. https://doi.org/10.1016/j.camwa.2018.08.033.
[24] K. Classens, T. Hafkamp, S. Westbeek, J.J.C. Remmers, S. Weiland, Multiphysical modeling and optimal control of material properties for photopolymerization processes, Addit. Manuf. 38 (2021) 101520. https://doi.org/10.1016/j.addma.2020.101520.
[25] K.C. Wu, J.W. Halloran, Photopolymerization monitoring of ceramic stereolithography resins by FTIR methods, J. Mater. Sci. 40 (2005) 71–76. https://doi.org/10.1007/s10853-005-5689-y.
[26] W. Rand, Applying Contemporary Statistical Techniques, Academic Press, 2003.

[27] S.P. Gentry, J.W. Halloran, Depth and width of cured lines in photopolymerizable ceramic suspensions, J. Eur. Ceram. Soc. 33 (2013) 1981–1988. https://doi.org/10.1016/j.jeurceramsoc.2013.02.033.
[28] I.K. Cingesar, M.-P. Marković, D. Vrsaljko, Effect of post-processing conditions on polyacrylate materials used in stereolithography, Addit. Manuf. 55 (2022) 102813. https://doi.org/10.1016/j.addma.2022.102813.
[29] M.N. Kumar, FEA Modelling of Weld-deposition based Additive Manufacturing for the Residual Stress Prediction, Thesis, 2014.
[30] K. Xu, Y. Chen, Curing Temperature Study for Curl Distortion Control and Simulation in Projection Based Stereolithography, in: Vol. 1A 34th Comput. Inf. Eng. Conf., American Society of Mechanical Engineers, Buffalo, New York, USA, 2014. https://doi.org/10.1115/DETC2014-34908.
[31] Y.-M. Huang, C.-P. Jiang, Curl Distortion Analysis During Photopolymerisation of Stereolithography Using Dynamic Finite Element Method, Int. J. Adv. Manuf. Technol. 21 (2003) 586–595. https://doi.org/10.1007/s00170-002-1317-z.